PNAS RESEARCH ARTICLE | ECOLOGY

Cooling outweighs warming across phenological transitions in the Northern Hemisphere

Yizhuo Li[a,b], Lin Meng[c,1], Andrew D. Richardson[d,e], Xuhui Lee[f], Annette Menzel[g,h], Jiafu Mao[i], Jen L. Diehl[d,e], and Anzhi Wang[a]

Affiliations are included on p. 11.

Edited by Steven Wofsy, Harvard University, Cambridge, MA; received January 23, 2025; accepted July 23, 2025

Vegetation phenology, i.e., seasonal biological events such as leaf-out and leaf-fall, regulates local climate through biophysical processes like evapotranspiration (ET) and albedo. However, the net surface temperature impact of these processes—whether ET cooling or albedo-induced warming predominates—and how the dominance changes across phenological transitions and regions remains poorly understood. Here, we investigated the effects of vegetation foliage on daytime land surface temperature (LST) following six phenological transitions, spanning from the start of season to end of season, in deciduous and mixed forests across the mid- to high-latitude Northern Hemisphere during 2013–2021 using multiple satellite products and ground observations. We quantified vegetation effect as the difference between observed LST and LST estimates from the Annual Temperature Cycle (ATC) model, representing a no-foliage scenario. We found that vegetation-induced cooling consistently outweighs warming following all phenological transitions except for the end of the season. Cooling intensity increased with vegetation greenness, ranging from 1.0 ± 0.5 °C (mean ± 0.15 SD) in 59% of forests after the start of the season (SOS) to 6.1 ± 0.8 °C in 89% of forests following the onset of maturity, before declining toward the end of the season. Over half of the regions experiencing cooling showed intensification of surface cooling with climate warming, suggesting an amplified vegetation-mediated cooling under future climate change. The findings provide a more precise understanding of the role of vegetation in modulating climate at the intraseasonal scale, highlighting the importance of integrating phenological impacts into climate adaptation strategies and Earth system modeling.

vegetation phenology | climate feedback | evapotranspiration | albedo

Significance

Vegetation plays a pivotal role in regulating Earth's climate through biophysical processes, yet its intraseasonal impacts on land surface temperature (LST) remain poorly understood. This study reveals that vegetation foliage exerts a dominant surface cooling effect during phenological transitions in mid- to high-latitude forests, with amplified cooling under climate warming in many regions. These findings provide insights into vegetation–climate interactions, emphasizing the critical role of phenology in temperature regulation. By quantifying the cooling effects of vegetation at an unprecedented intraseasonal scale, the results highlight the potential of vegetation management strategies, such as afforestation and seasonal planning, to mitigate climate warming and enhance ecosystem resilience, offering actionable guidance for sustainable climate adaptation.

Vegetation phenology, a highly sensitive biological indicator to climate change, provides crucial biophysical feedback to the climate system by altering energy and water exchange between the land surface and atmosphere (1–3). Climate warming has lengthened the growing season, causing earlier leaf emergence and mostly later senescence in recent decades (4–8). These phenological changes impact the seasonality of surface temperature mainly through two competing biophysical processes that affect the energy balance: changes in solar radiation absorption due to altered albedo and variations in energy distribution caused by the modified evapotranspiration (ET) (9–12). Phenology-induced changes in surface temperature seasonality have critical implications on ecosystem processes and feedback mechanisms, especially under a changing climate (13–16). However, the direction and magnitude of vegetation impact on climate and how it evolves across phenological transitions throughout the growing season are largely unclear, leading to uncertainties in predicting vegetation–climate interactions under climate change (17, 18).

The net thermal impacts of vegetation are influenced by biophysical processes that vary spatially and seasonally (11). Spatially, in cold boreal regions with winter snow cover, earlier spring greening drastically reduces albedo, leading to more shortwave radiation absorption and potentially warming, although with large spatial variation (19). Conversely, tropical regions experience a net cooling effect from increased ET after green-up, which offsets the warming from reduced albedo (20–22). With increasing latitude, the climatic feedback of spring greening may shift from net cooling to warming (21, 23), suggesting a dependency on broader geographic and climatic variations. In temperate regions, however, the net effect of vegetation on surface temperatures remains controversial (14, 24, 25) due to competing albedo and ET effects (26, 27) as well as overriding effects of large-scale atmospheric circulations (28, 29) and soil moisture variability (30). This controversy is further compounded by the limitations of in situ measurements or uncertainties in coupled land–atmosphere models, leaving it unclear whether the large-scale thermal impacts of vegetation observed through direct measurements align with previous findings (7).

Author contributions: Y.L. and L.M. designed research; Y.L. and L.M. performed research; Y.L., L.M., and J.L.D. analyzed data; and Y.L., L.M., A.D.R., X.L., A.M., J.M., J.L.D., and A.W. wrote the paper.

The authors declare no competing interest.

This article is a PNAS Direct Submission.

[1]To whom correspondence may be addressed. Email: lin.meng@vanderbilt.edu.

This article contains supporting information online at https://www.pnas.org/lookup/suppl/doi:10.1073/pnas.2501844122/-/DCSupplemental.

Published September 8, 2025.

Seasonally, the temperature effect may shift from albedo-induced warming in spring and autumn to ET cooling in summer with phenological transitions (26, 31). This shift occurs because the spring leaf-out and autumn leaf-fall processes reduce albedo, increasing the absorption of solar radiation and subsequent warming (21, 32, 33). However, the phenological variability following leaf emergence can reduce maximum surface temperatures (30, 34, 35). Therefore, in summer, high solar radiation and considerable canopy greenness significantly enhance ET, which generates a strong cooling effect that offsets the warming observed in other seasons (36) as long as there are no drought constraints (34). The timing of these temperature shifts is likely to vary annually due to interannual variations in phenological transitions, which can differ by several days, but this variation remains poorly understood (34, 37). Furthermore, the extent of these impacts across phenological transitions—such as leaf out, active growth, senescence, and dormancy—and their variability under different climate conditions are not fully investigated (18, 38–40). This lack of understanding of vegetation effects across phenological transitions could lead to challenges in accurately predicting the influence of vegetation on regional and global temperature patterns at the intra-seasonal scale (41, 42).

Here, we quantify the impact of vegetation on land surface temperature (LST) across six phenological transitions in deciduous and mixed forests over the mid- and high-latitudes across the Northern Hemisphere (30 to 70°N) from 2013 to 2021. The objectives are to 1) identify the immediate vegetation impact on LST after each phenological transition, 2) quantify the cumulative vegetation effect on LST throughout the growing season across climate types, and 3) examine the magnitude of changes in LST over time in response to climate warming across background climates. We analyze global patterns using daytime LST data from the Moderate Resolution Imaging Spectroradiometer (MODIS) and phenological indices from the Visible Infrared Imaging Radiometer Suite (VIIRS) Global Land Surface Phenology Product (GLSP). We also validate the results using LST observations from 17 deciduous and mixed forest sites from AmeriFlux, integrated with ground phenological data from the PhenoCam Network in the United States. To isolate the vegetation effect on LST, we first estimated the reference daily temperature time series—representing the scenario without the impact of vegetation phenology dynamic—by fitting a sinusoidal Annual Temperature Cycle (ATC) model to nongrowing season LST (i.e., LST_{ATC}; see *Materials and Methods*). We then compared this daily LST_{ATC} with actual observed LST (LST_{Obs}) during the growing season, which includes the vegetation effects. The differences between these two LST time series across phenological transitions were treated as vegetation effects on LST: negative for cooling and positive for warming. We examined the vegetation effect across six phenological transitions from VIIRS product: Start of Season (SOS), Mid-Greenup Phase (MGP), Greenness Maximum Onset (GMO), Greenness Decrease Onset (GDO), Mid-Senescence Phase (MSP), and End of Growing Season (EOS), along with two events from PhenoCam Network: green-up onset and dormancy. We tested two competing hypotheses: 1) vegetation exerts a dominant warming effect across phenological transitions, primarily driven by reduced albedo and consequently enhanced radiation absorption during the growing season, and 2) vegetation exerts a dominant cooling effect across phenological transitions, driven by ET (Fig. 1). We further hypothesized that in regions with sufficient water supply, where cooling effects dominate, cooling intensifies from SOS to GMO and then diminishes toward EOS. Conversely, in regions dominated by warming effects, warming decreases from SOS to GMO and increases again as EOS approaches.

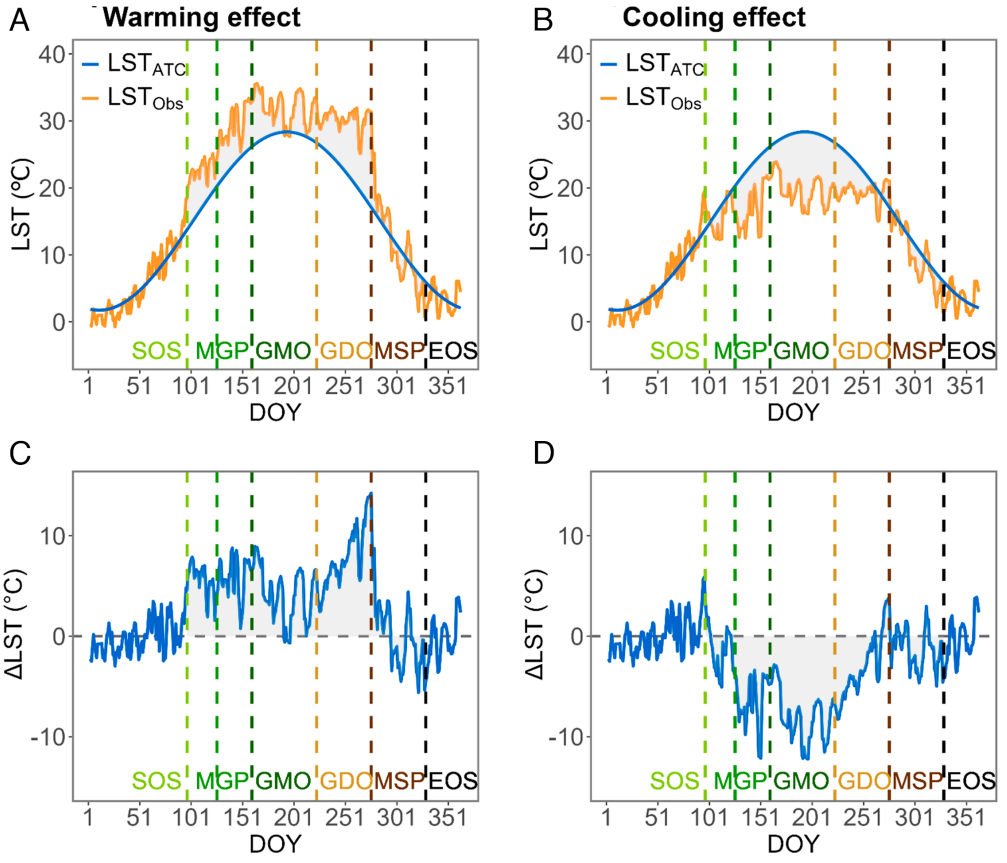

Fig. 1. Two competing hypotheses regarding the vegetation effect on land surface temperature (LST) across six phenological transitions. (*A*) Warming effect across phenological transitions. (*B*) Cooling effect across phenological transitions. LST_{ATC}: estimated reference LST derived from the Standard Annual Temperature Cycle (ATC) model, representing the scenario without vegetation effects. LST_{Obs}: daily observed LST from MODIS or AmeriFlux, which includes the vegetation effects. (*C* and *D*) The difference between LST_{ATC} and LST_{Obs} (negative ΔLST represents vegetation cooling effect). The shaded areas highlight the cumulative ΔLST during the growing season. Vertical dashed lines represent the six phenological transitions: the start of the season (SOS), mid-greenup phase (MGP), greenness maximum onset (GMO), greenness decrease onset (GDO), mid-senescence phase (MSP), and the end of the growing season (EOS).

Results

Prevalent Immediate Cooling Effect After Phenological Transitions. We assessed the intraseasonal changes in vegetation impact on LST over the 5 d following each phenological transition (Fig. 2; *Materials and Methods*). The global satellite results revealed a marked immediate cooling effect following all phenological transitions except for EOS, with the magnitude of the effects intensifying from the start to the middle of the growing season and then gradually declining toward the end. Northern Asian forests maintained a robust year-round cooling effect across all phenological transitions, while mid- and high-latitude forests in Europe and North America showed discernible seasonal variations. Following SOS, 59% of the study area exhibited a cooling effect, while 41% showed a warming effect, with a mean cooling of −0.99 ± 0.54 °C (mean ± 0.15 SD; Fig. 2*A*). Regions showing a warming effect included the west coast and northern North America, including Canada's northern forests, as well as parts of Northern and Eastern Europe and Central Asia. In contrast, as vegetation greening progressed from MGP to GMO, cooling intensified across the Northern Hemisphere, particularly in southeastern North America, Southern Europe, Eastern Asia, and regions near 30°N, peaking at GMO with −6.06 ± 0.78 °C observed in 89% of forests. This substantial cooling gradually declined, from a high net cooling effect of −5.44 ± 0.78 °C observed in 87% of forests at GDO to a moderate cooling of −2.63 ± 0.48 °C at MSP. After the EOS, a moderate warming effect (−0.17 ± 0.36 °C, Median: 0.06 °C) was noted across 51% of mid- and high-latitude forests (Fig. 2*F*).

We observed similar patterns on both sides of the growing season based on ground measurements. Among the 17 AmeriFlux sites, 10 (59%) sites showed a warming effect on LST following green-up, with a temperature increase of 0.45 ± 0.32 °C on average (*SI Appendix*, Fig. S1). Similarly, 7 sites (41%) showed a warming effect following green dormancy, with a temperature increase of −0.37 ± 0.27 °C. We also compared near-surface air temperature (Ta) and LST from AmeriFlux, as well as their vegetation-induced changes (ΔTa and ΔLST), and found a strong positive correlation (*SI Appendix*, Fig. S12). This demonstrated that LST reliably captured broader patterns in Ta, and the vegetation impact on LST reflected similar trends in Ta. During the growing season, the cooling effect of vegetation (both ΔTa and ΔLST) increases after

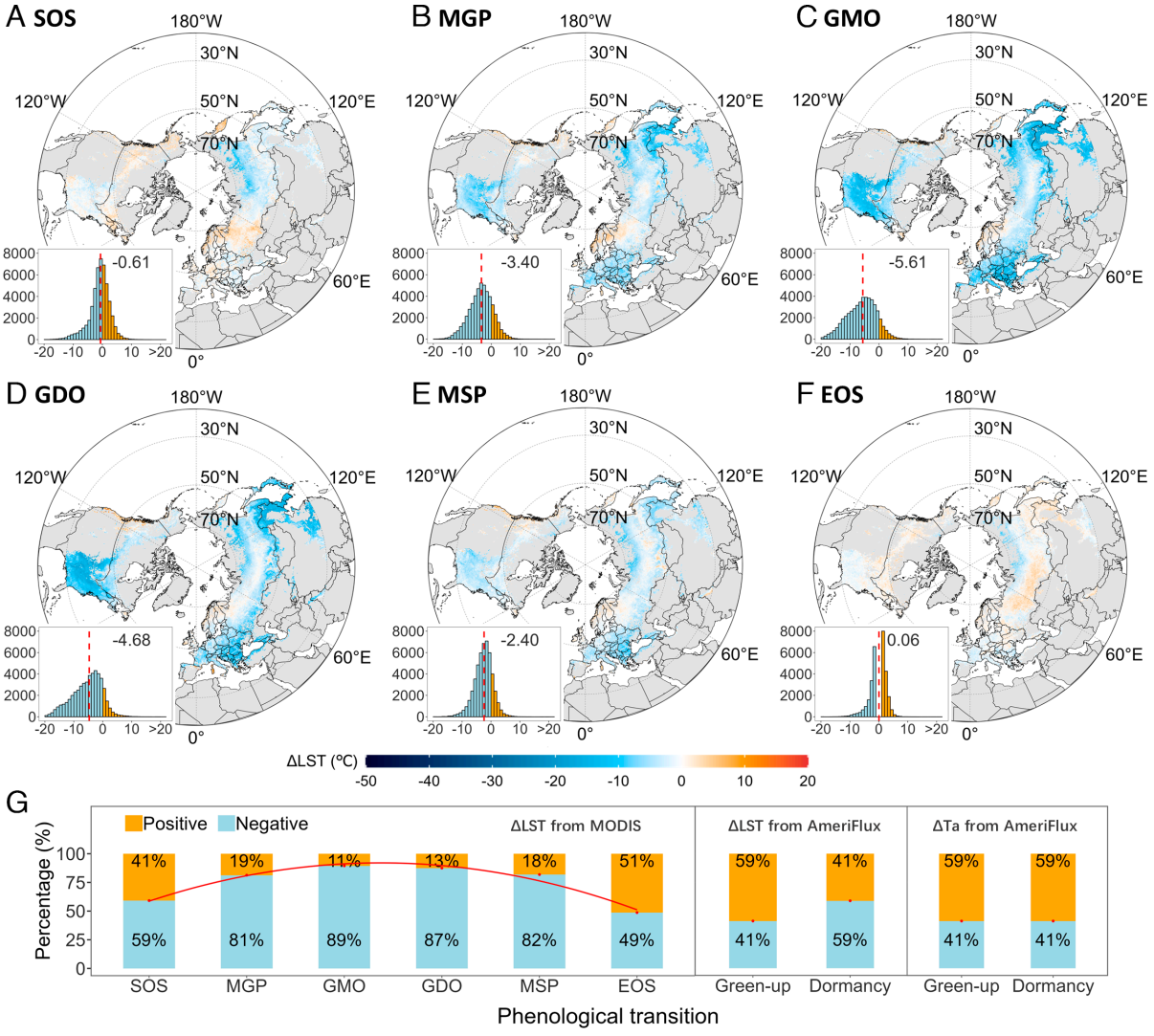

Fig. 2. Prevalent vegetation cooling effect following phenological transitions across the Northern Hemisphere from 2013 to 2021 based on satellite and ground measurements. (*A*–*F*) Spatial distribution of the 5-d mean LST difference (ΔLST) between LST_{ATC} and LST_{Obs} from MODIS following each phenological transition. The inserted figures show ΔLST histograms, with the red dotted line and texts indicating the median values. (*G*) Percentages of study areas with positive and negative ΔLST after phenological transitions. The red curve represents the variation in the proportion of forests exhibiting a cooling effect following VIIRS-derived phenological transitions: the SOS, MGP, GMO, GDO, MSP, and EOS. The two groups of rightmost bars represent AmeriFlux site-level ΔLST and ΔTa (between ATC-estimated Ta and observed Ta) following PhenoCam green-up and dormancy, respectively. Negative ΔLST (ΔTa) represents the vegetation cooling effect.

green-up, peaks with maximum ET, and declines toward dormancy—aligning with seasonal ET dynamics at AmeriFlux sites (*SI Appendix,* Fig. S13*A*). Elevated ET consistently leads to greater cooling (more negative ΔLST) across five sequential phenological stages spanning from green-up to dormancy (−0.71 °C per 1 mm/d; *SI Appendix,* Fig. S13*B*), providing direct evidence on the direct biophysical mechanism through which vegetation regulates surface energy balance via evaporative cooling. These findings supported the hypothesis that pronounced increasing ET-driven cooling predominantly counteracts the warming effects throughout the growing season, particularly during peak greenness. In contrast, warming effects tend to dominate at the beginning and EOS.

The magnitude of cooling (ΔLST) from the MGP to MSP slightly increased from 2013 to 2021 across the Northern Hemisphere, indicating a stronger ET-induced cooling effect over the years (Fig. 3 *B*–*E*). Conversely, the magnitude of warming at EOS also intensified over the years (positive slopes of ΔLST), suggesting a moderate warming trend at the EOS (Fig. 3*F*). Notably, in 2015, 2016, and 2021—years marked by extreme heat in North America—the cooling impact of vegetation reached unprecedented levels, with ΔLST post-GDO of −8.24 to −10.94 °C—an effect not observed as pronounced in Eurasia (Fig. 3*D* and *SI Appendix,* Fig. S4). This indicates a heightened response of vegetation to extreme temperature events.

Cumulative Vegetation Impact on Temperature Across Climate Types. To investigate the accumulated effect of vegetation growth on LST during the growing season and its variation across climate types, we quantified the sum of ΔLST between every two phenological transitions and for the entire growing season. During the entire growing season, the total cumulative cooling effect was on average −753 ± 112 °C d based on MODIS observations and −622 ± 99 °C d based on AmeriFlux data, with significant geographical variability (Fig. 4 *A* and *D*). A pronounced cooling effect was observed in 88% of the study areas, including southeastern North America, Southern Europe, and Eastern Asia (Fig. 4*C*). Similarly, cumulative cooling impacts were observed at 14 sites (82%) based on ground measurements (*SI Appendix,* Fig. S1). Conversely, forests in the western coastal regions of North America, along with certain areas in Northern and Eastern Europe and Central Asia, exhibited a cumulative warming effect (12% of the study areas) (Fig. 4*C*). This cumulative cooling effect indicates the ET-cooling effect within the growing season outweighed the warming at the start and EOS, resulting in a prevailing net cooling effect over the entire growing period.

The cumulative vegetation impacts on LST varied largely with background climates. Across temperature-based Köppen–Geiger climate classifications (hot, warm, cool summers, and extremely continental conditions), in both warm temperate and cold regions, the cumulative cooling effect was most pronounced in hot summer climates, followed by extremely continental conditions, and was the least under cool summer climates (Fig. 4 *E*–*K*). Specifically, in cold climates, vegetation in hot summer (DXa) exhibited the most significant cumulative cooling effect throughout the growing season, averaging −1,867 ± 93 °C d, followed by that in extremely continental conditions (DXd, −1268 ± 33 °C d) (Fig. 4 and *SI Appendix,* Table S5). Forests in cold regions with warm summers (DXb) and cool summers (DXc) showed the least cooling effects, only ~46 and 20% of those observed in DXa, respectively. In warm temperate climates, vegetation exhibited a substantial cumulative cooling effect in hot summer climates (CXa: −1737 ± 125 °C d) and warm summer climates (CXb: −829 ± 124 °C d), but a cumulative warming effect in cool summer climates (CXc: 352 ± 55 °C d). Seasonally, more than half of the accumulated cooling effect across the Northern Hemisphere occurred during the GMO-GDO period (−437 ± 61 °C d), indicating the strongest ET-induced cooling during peak greenness (*SI Appendix,* Table S5). The accumulated cooling in this GMO-GDO period was most pronounced in hot summer climates (CXa: −986 ± 66 °C d, DXa: −1,113 ± 49 °C d), while relatively modest warming (144 ± 26 °C d) was observed, particularly in temperate climates regions with a cool summer climate type (<1% of study areas). Across Ameriflux sites, the cooling effect varied in a similar pattern across climate types. In humid conditions, a notable

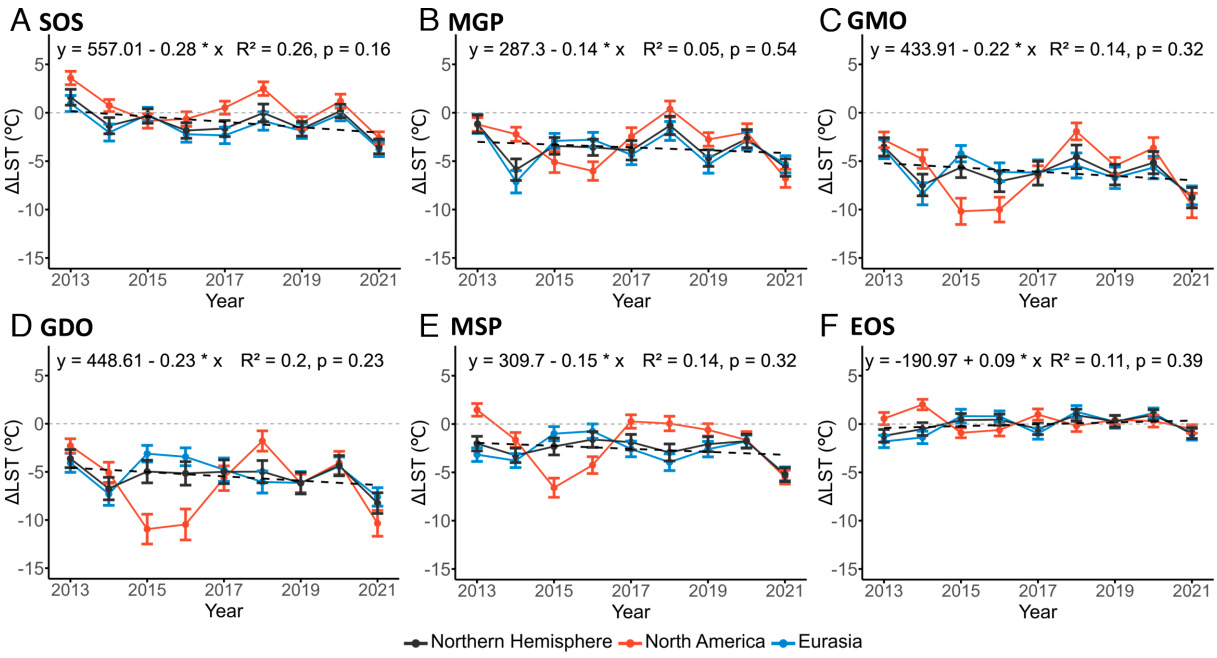

Fig. 3. Annual variation of LST difference (ΔLST) between LST_{ATC} and LST_{Obs} from MODIS following each phenological transition across the Northern Hemisphere, North America, and Eurasia from 2013 to 2021. (*A*–*F*) represent the 5-d mean ΔLST following the phenological transitions SOS, MGP, GMO, GDO, MSP, and EOS, respectively. Error bars indicate the region-wide spatial variation (± 0.15 of the SD). Regression lines and corresponding coefficients of determination for the Northern Hemisphere are reported as black dashed lines and annotated in the figures.

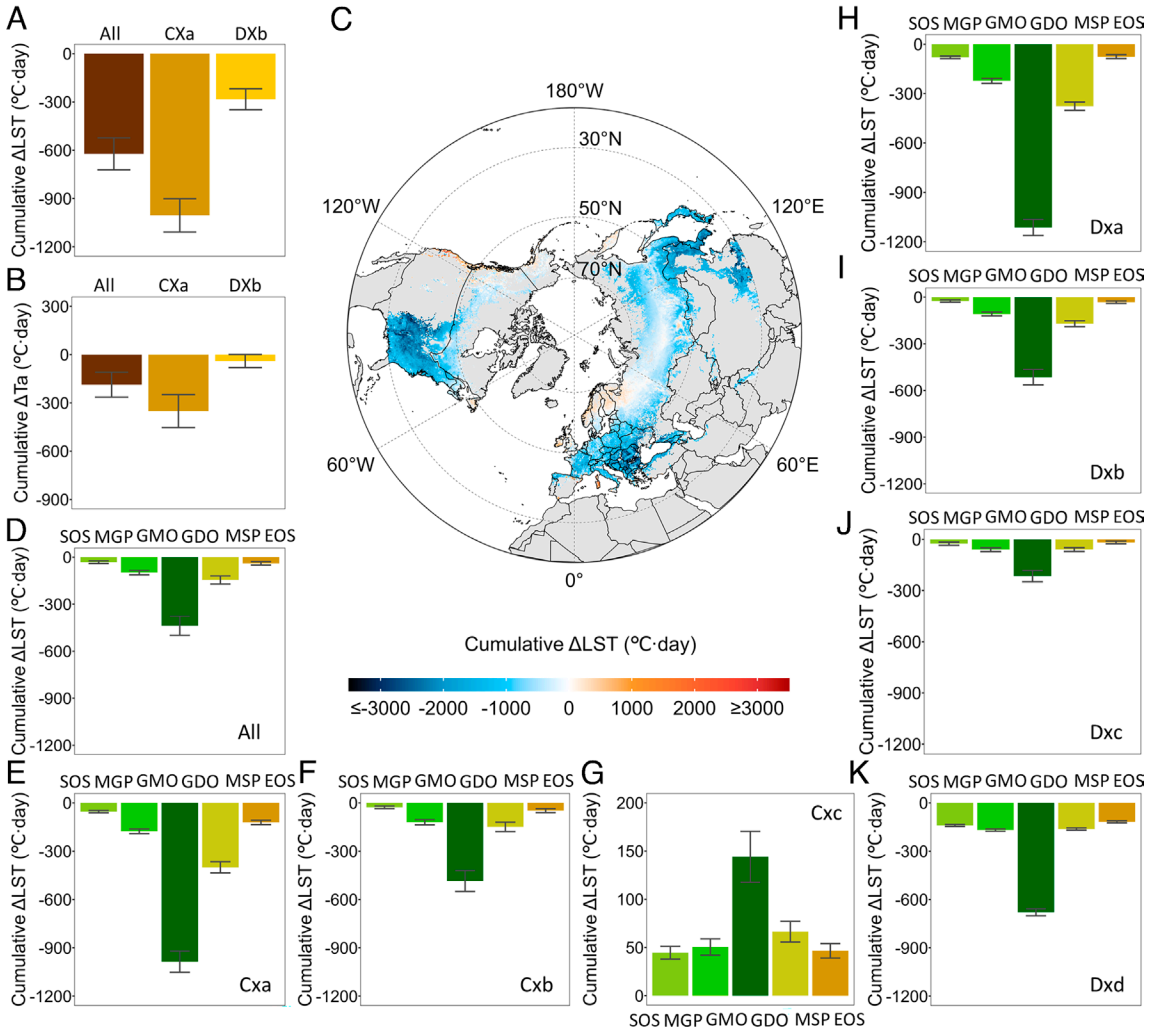

Fig. 4. Cumulative vegetation effects on LST throughout the entire growing season across climate types in the Northern Hemisphere from 2013 to 2021 based on satellite and ground measurements. (*A* and *B*) represent the average cumulative ΔLST (between ATC-estimated LST and observed LST) and ΔTa (between ATC fitted Ta and observed Ta) from green-up to dormancy at AmeriFlux sites across two Köppen–Geiger climate types classified by temperature: warm temperate climates with hot summers (CXa) and cold climates with warm summers (DXb), respectively. (*C*) Spatial distribution of the cumulative ΔLST between LST_{ATC} and MODIS LST_{Obs} across the Northern Hemisphere. (*D*) Average cumulative ΔLST between LST_{ATC} and MODIS LST_{Obs} across phenological transitions. (*E*–*G*) Similar to c but for each Köppen–Geiger climate type. (*D-F*) represents warm temperate climates with hot (CXa), warm (CXb), and cool summers (CXc). (*H*–*K*) represents cold climates with hot (DXa), warm (DXb), cool summers (DXc), and extremely continental conditions (DXd). Negative cumulative ΔLST (ΔTa) represents the cooling effect. The error bars represent the spatially averaged ± 0.15 of the SD.

strengthening of the cooling effect on LST was observed particularly with warmer conditions (−1005 ± 103 °C d in CXa versus −283 ± 65 °C d in DXb), with a similar pattern observed for Ta (Fig. 4 and *SI Appendix,* Tables S8 and S9). Across wetness conditions (fully humid, summer dry, and winter dry climate types): The cumulative cooling impact was greatest in winter dry environments (CwX, DwX), followed by fully humid conditions (CfX, DfX), and was the least in summer dry conditions (CsX, DsX) in both warm temperate and cold regions (*SI Appendix,* Fig. S5 and Table S6).

The cumulative vegetation impacts on LST also varied with forest types from both satellite and in situ observations (*SI Appendix,* Fig. S6). Deciduous broadleaf forests showed consistently strong effects across climates, with the greatest cooling in CXa (−1987 ± 94 °C d) and strongest warming in CXc (549 ± 49 °C d) during the growing season. Mixed forests exhibited the weakest effects (−1500 ± 67 °C d in DXa; 241 ± 53 °C d in CXc), followed by deciduous needleleaf forests. Overall, both deciduous and mixed forests induced pronounced cooling in hot summer climates (DXa, CXa), but warming in cool summer conditions (CXc). Needleleaf forests showed variable cooling with the strongest effect in Dxd climates (−1278 ± 29 °C d).

Temperature Sensitivity Across Background Climates. To understand the changes in vegetation impact on LST under future climate change, we examined the sensitivity of vegetation-induced ΔLST to background climate, characterized by average annual temperatures, using pixel-level linear regression. The regression slope was used to quantify the temperature sensitivity (D_T). Positive D_T, indicating an increase in warming or a reduction in cooling with rising temperatures, was observed in northwestern and eastern North America and across inland Eurasia (Fig. 5). Conversely, negative D_T, indicating stronger cooling or weakened warming with rising temperatures, was notably observed in southeastern North America, Southern Europe, and Eastern and Western Asia, particularly around 30°N.

We categorized the vegetation effect on LST (ΔLST) and its temperature sensitivity (D_T) into four categories: W-P (warming effect that intensifies with rising temperatures), W-N (warming effect that weakens with rising temperatures), C-P (cooling effect that weakens with warming), and C-N (cooling effect that intensifies with warming) (Fig. 6). Overall, C-N proportions exceeded C-P, while W-P and W-N were similar but much lower, indicating that regions where cooling intensified with rising temperatures were

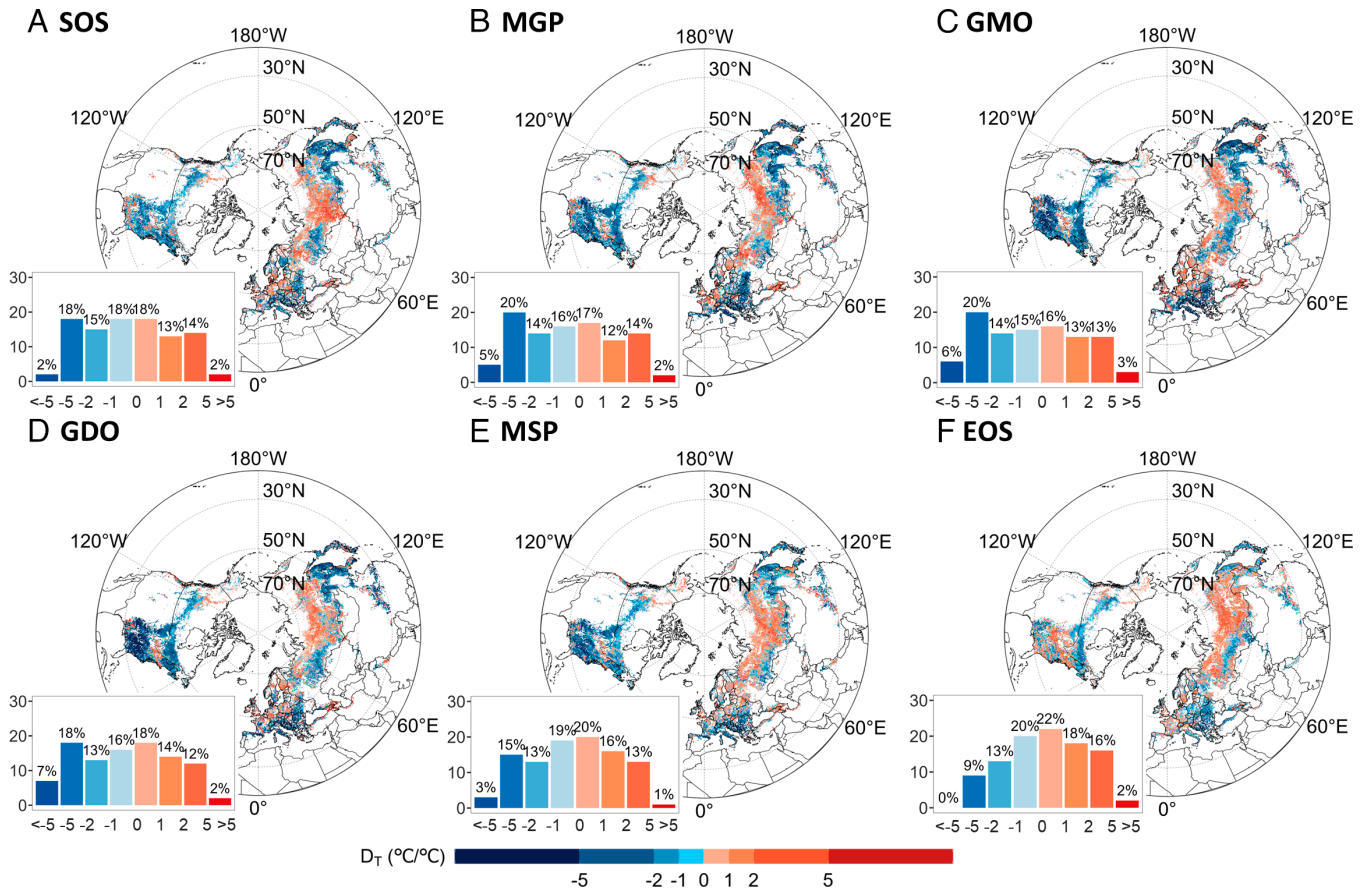

Fig. 5. Temperature sensitivity (D_T) across the Northern Hemisphere from 2013 to 2021. (*A–F*) Spatial distribution of DT following the phenological transitions SOS, MGP, GMO, GDO, MSP, and EOS. The lower-left figure shows the histogram of D_T after each phenological transition. D_T represents the sensitivity of vegetation-induced ΔLST to background climate conditions, characterized by average annual temperatures. Positive D_T indicates stronger warming or weakened cooling with rising temperatures. Negative D_T indicates stronger cooling or weakened warming with rising temperatures.

more extensive than those where cooling weakened or warming strengthened with rising temperatures. Our in situ analysis across AmeriFlux sites further revealed that warmer years were associated with higher growing-season ET ($P < 0.05$, *SI Appendix*, Fig. S13*C*), highlighting vegetation's amplified cooling capacity under hotter conditions. This pattern aligns with our satellite-based findings and supports previous studies showing that warming increases ET (43). The proportions of these four categories evolved throughout the growing season. After SOS, positive and negative D_T overlapped equally with regions of cooling effect, resulting in 30% of C-N primarily in southeastern North America, Southern Europe, Eastern Asia, and near the 30°N latitude, and 30% of C-P, mainly in central Europe and Northern Asia. From SOS to GMO, the proportions of both C-N and C-P increased, with C-N rising more significantly (to 52% at GMO). As vegetation senescence progressed, the proportions of C-N and C-P declined, with C-N eventually surpassing C-P after EOS. In contrast, W-N accounted for 23% at SOS, predominantly in the northern forests of North America and Western and Eastern Europe, while W-P accounted for 17%, mainly in southeastern North America and Eastern Europe. As vegetation greenness increased, the proportions of both W-P and W-N rapidly declined, reaching their lowest at GMO (W-P: 5%; W-N: 4%). During senescence, both slightly increased, ending with similar proportions at EOS (W-P: 27%; W-N: 26%).

Discussion

The prevalent net cooling effect from SOS to MSP, and a net warming effect at EOS transitions across the Northern Hemisphere, reported in this study, highlight the substantial dynamic shifts in vegetation regulation on surface temperature across phenological transitions. Although the relationship between LST and Ta can be influenced by turbulent coupling, canopy structure, and surface energy balance (44–48), our results show that LST reliably captures broader spatial and seasonal patterns in Ta. This suggests that vegetation-driven changes observed in LST can serve as a reliable proxy for air temperature dynamics, which is critical for assessing land–atmosphere interaction. The rapid increase in foliage cover induces both radiative (surface albedo) and nonradiative (ET) biophysical alterations, resulting in shifts in solar radiation absorption and the partitioning of energy between sensible and latent heat (6, 49, 50). The competition of these two factors governs the seasonal dynamic of the vegetation impact on LST across regions (18). Forests dissipate sensible heat more efficiently than open landscapes due to the transition from bare ground to tall vegetation (25, 51), however, the impact of leaf-on and -off on surface roughness in deciduous forests is minimal (50, 52). Before the start of the growing season, snow-covered soils and bare branches with their higher albedo reflect more solar radiation compared to vegetation and wet soils, which have lower albedo (53, 54), especially at high latitudes in early spring (55, 56). Subsequently, the unfolding of leaves results in a strongly decreased albedo, thereby leading to a warming effect (54, 57). The substantial greening expansion increases ET, enhancing surface evaporative cooling and surpassing the albedo-related warming earlier in the growing season, resulting in net cooling after MGP. This net cooling effect peaks during the leaf-peaking season (GMO to GDO). As canopy density increased during this phase, albedo rose from low spring values to seasonal

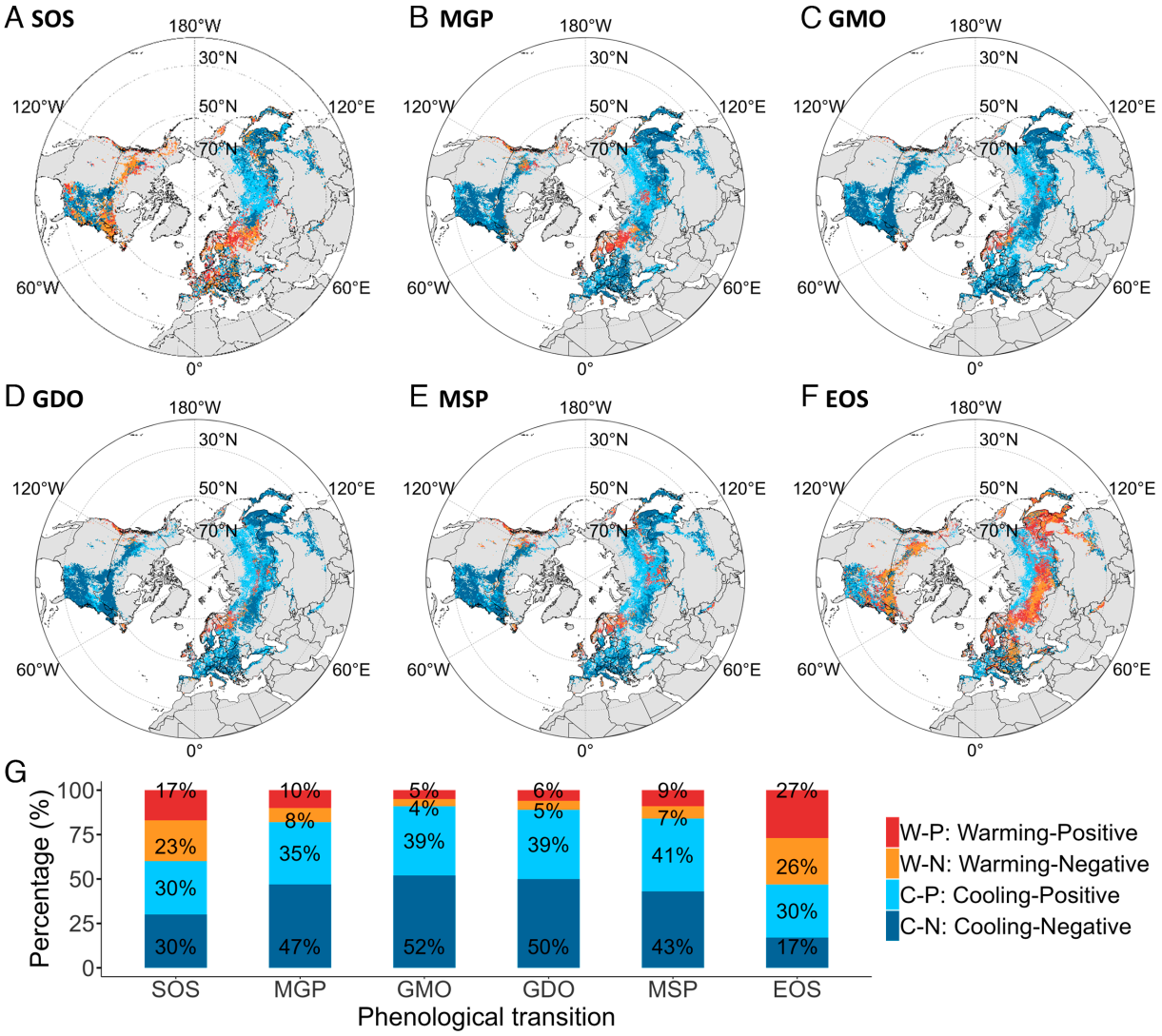

Fig. 6. Temperature sensitivity of the vegetation impact on LST across the Northern Hemisphere from 2013 to 2021. (*A*–*F*) Spatial distributions of the vegetation effect on LST and its temperature sensitivity for the six phenological transitions SOS, MGP, GMO, GDO, MSP, and EOS. Cooling-Negative (C-N) means a vegetation cooling effect that intensifies with rising temperatures. (*G*) Percentages of the vegetation effect on LST and its temperature sensitivity for the six phenological transitions across the Northern Hemisphere.

peaks as the foliage expanded in deciduous forests (33), resulting in a slightly strengthened cooling. During leaf senescence and shedding, canopy gaps widened and darker optical properties of stems were exposed, enhancing light penetration and reducing foliage interception (58). Specifically, although albedo increased slightly in the early fall before decreasing as leaves turned bright yellow or brown, leaf reflectance and transmittance in the visible wavelengths increased as a result of the rapid destruction of chlorophyll (33, 59). The subsequent decline in photosynthetic capacity and water content further reduced albedo (58, 60), accompanied by diminished ET-driven cooling, leading to a return to moderate warming. Our findings align with previous findings on intraseasonal trends of vegetation effects (18, 21, 23, 36), providing more detailed evidence across phenological transitions.

Following the SOS, vegetation exhibits distinct warming (40%) and cooling (60%) effects, revealing two typical patterns of how vegetation-induced ΔLST responds to interannual temperature variation across phenological transitions (Fig. 6). In high-latitude regions (e.g., Central Europe, Eastern Europe, and Northwestern Asia), vegetation initially causes post-SOS warming, with varying sensitivity (W-N, W-P). This warming is partly attributed to concurrent snowmelt, which strongly decreases land surface albedo and thus causes warming. As greening intensifies, ET-driven cooling dominates (32, 37), gradually replacing much of the warming. About half of the regions directly shift from warming post-SOS to consistent cooling-negative (C-N) after GMO, while 31% transition to C-P, likely due to constrained ET cooling under dry conditions (9, 61) or intensifying drought events. In contrast, in mid-latitude regions with hot summers and fully humid conditions, such as Southeastern North America and Northern Asia, rising temperatures and rapid greening enhance ET-induced cooling, starting with C-P during SOS. As foliage density increases, 34% of C-P transition to C-N post-MGP, excluding unchanged pixels (59%), marking the largest shift. Similarly, 27% of unchanged C-P transition to C-N post-GMO, suggesting that enhanced cooling potential (negative D_T) by vegetation may lead to increased soil water loss as temperatures rise (62, 63), resulting in significant cooling. However, during peak season, C-P proportions increase, indicating that converted ET-induced cooling potential may be limited due to increased water deficits driven by ET losses (64), more frequent drought events, and the advanced SOS (65–67). Moreover, the positive effect of vegetation greenness on ET may be attributed to the delayed phenology (68) (*SI Appendix*, Table S3). This trend, with amplified cooling during peak season, highlights the complex ecosystem responses to climate warming (Fig. 7).

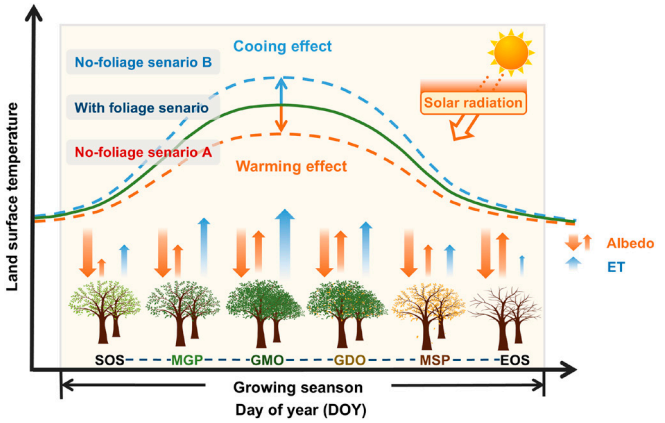

Fig. 7. The effects of vegetation foliage on LST across phenological transitions under cloud-free conditions. The orange and blue dashed lines represent LST derived from the Standard ATC model, representing two possible scenarios without foliage. The green solid line represents the MODIS-observed LST, a scenario with the vegetation foliage effects. The blue upward arrow and the orange downward arrow represent the cooling and warming effects of vegetation foliage, respectively. The thickness and size of the arrows for evapotranspiration (ET) and albedo represent the magnitude of their effects driven by phenological transitions. The six phenological transitions are the SOS, MGP, GMO, GDO, MSP, and EOS.

We found compelling evidence that warmer conditions amplified the magnitude of vegetation-driven cooling effects. For instance, during the extremely warm years of 2015–2016 and 2021, significant cooling effects were observed in the United States, where most regions were characterized by C-N (Fig. 3 and *SI Appendix,* Figs. S4 and S10). This was probably due to vegetation greening and an extended growing season, which are expected to prolong the period of vegetation-driven cooling (6, 69). In addition, the magnitude of the cooling effect (ΔLST) increased from 2013 to 2021, indicating an amplified cooling effect as the climate warms. Seasonally, the cooling effect of vegetation also peaks during the period of maximum greenness, from GMO to GDO, coinciding with peak summer temperatures.

The magnitude of cumulative vegetation impacts on LST underscores the critical influence of background climates. In regions like Southeastern North America, characterized by hot, fully humid summers (CXa) (70), stronger cooling accumulation during the growing season is observed compared to high-latitude areas with warm, dry summers (Cxb), despite both being C-N. This suggests that humidity is essential for enhancing ET-cooling, particularly in warm temperate climates where photosynthetic activity is heightened (61, 71, 72) (*SI Appendix,* Fig. S7*B*). Conversely, cool, humid climates (CXc), like those in western coastal regions of Canada and parts of Scotland, Norway, and Sweden, exhibit cumulative warming. This is probably attributed to reduced vegetative activity from lower temperatures and shorter growing seasons (73). Darkened leaves can reduce transmittance as the canopy develops, which results in a decrease in albedo absorbing excess solar radiation (18, 41, 60, 74), leading to intense warming as well. It is consistent with previous findings that albedo-induced warming surpasses ET-cooling in specific humid regions (59), where increased cloud cover reduces outgoing longwave radiation (50). However, the positive D_T in CXc during peak greenness suggests that increased ET-driven cooling with rising temperatures can partially counteract the warming effect. Similarly, cumulative cooling in cold climate regions reflects similar patterns, with greater cooling in areas with higher summer background temperatures. This is supported by the findings that DXa regions exhibit the most cumulative cooling, followed by DXb and DXc (Fig. 4 *H–J*). Dry winters, followed by summer rainfall and abundant sunlight, significantly boost photosynthesis and transpiration (75), driving seasonal vegetation spurts (38) and contributing to substantial ET-induced cooling in DXd regions with continental characteristics in high-latitude areas (Fig. 4*K*). Under CXa and CXb with humid conditions, the stronger cooling in DXa and DXb likely results from greater albedo increases in northern deciduous forests at higher mid-summer solar elevations (33), along with restricted ET in relative humidity climates. However, in cold climate regions with dry summer conditions, enhanced ET can exacerbate soil water loss under dry conditions (62, 76), which can increase vapor pressure deficits and further exacerbate soil moisture deficits (77–79) over subsequent phenological stages. Along with the dominant radiative forcing (80, 81), the water deficit may amplify warming sensitivity and reduce cooling impact at the start of the growing season. The expansion of foliage cover subsequently mitigates negative temperature sensitivity probably by enhancing soil water transfer and latent heat release (82), though this effect weakens after senescence (*SI Appendix,* Figs. S7*C* and S8*C*). The findings on the varying vegetation phenological transitions' impact on LST across climate backgrounds are particularly critical for implementing effective vegetation management strategies under increasingly frequent and severe extreme droughts (83, 84).

Vegetation-induced cooling varied across forest types due to differences in physiological and structural traits (*SI Appendix,* Fig. S6). Deciduous broadleaf forests, containing more anisohydric species that maintain transpiration under higher VPD, exhibited the strongest cooling, supported by dense canopies and high stomatal conductance sustaining transpiration and reducing radiation absorption (38, 85, 86). Needleleaf forests, including more isohydric species with conservative water use, cooled less effectively due to lower albedo, greater roughness, and early stomatal closure under high VPD (63, 87–89). Composed of species with divergent water-use strategies, mixed forests showed asynchronous VPD-temperature responses and higher canopy transmittance, weakening transpiration-driven cooling (63, 90). Under cooler mesic conditions experiencing drier years (e.g., Cxc), reduced stomatal conductance in response to water stress—particularly in broadleaf species—further suppressed ET and amplified warming (86, 91, 92). While structurally resilient (93), mixed forests may benefit from increased broadleaf dominance to improve climate buffering (87), though their heat and drought sensitivity calls for careful management. As VPD and climate extremes intensify, species-specific mechanisms must be understood to guide forest-based climate strategies.

As climate change and extreme events affect the timing of leaf onset and senescence (84), examining vegetation's impact on LST across phenological transitions provides essential insights for improving the accuracy of climate models in capturing the biophysical impact across these shifts. Our findings highlight the inadequacy of traditional aggregate analyses in capturing transient but significant phenological impacts on LST (28, 31). Future research should prioritize high temporal resolution studies that can effectively capture the thermal dynamics associated with early or delayed leaf-out and prolonged growing seasons. It is also critical to investigate the roles of other climatic drivers, such as photoperiod, humidity, and chilling intensity, as well as biotic factors, in shaping vegetation's temperature effects. These studies can provide new insights into how vegetation moderates surface energy balance during critical phenological stages, such as the shoulder seasons when vegetation dynamics rapidly change (28, 94). Addressing these questions will also enhance our ability to design climate adaptation strategies, such as optimizing land management practices or deploying nature-based solutions to mitigate climate extremes.

Our study applied the ATC model to isolate the impact of vegetation on LST, based on the assumption that temporal LST

variations are largely driven by solar radiation flux (95–97). The resulting LST_{ATC} reflects the annual LST without foliage cover, providing a baseline for comparison with the actual scenario of vegetation impact. We acknowledge, however, that the actual annual surface temperature cycle is more complex, influenced by short-term factors such as weather fluctuations, snow/ice cover, and vegetation or soil conditions. In snow-covered regions, the model assumes a static surface and accounts for snow-related albedo year-round when simulating no-foliage scenarios, potentially causing a slight overestimation of warming or underestimation of cooling during the growing season. Nevertheless, these limitations do not alter the observed early season transition from warming to cooling, nor the sensitivity analysis of daytime LST impacts under climate warming. In addition, vegetation–cloud feedback may indirectly link phenology to surface energy balance, e.g., enhanced ET following leaf-out can contribute to increased cloud formation (29, 98), which in turn may reduce incoming shortwave radiation and moderate surface warming. However, our comparison between LST and ΔLST derived from cloud-free and full time series observations suggests that cloud presence does not substantially alter the detected vegetation-induced temperature signals, supporting the robustness of our conclusions (*SI Appendix,* Fig. S14). Future work should integrate phenological dynamics with cloud processes and land–atmosphere interactions to quantify vegetation impacts on LST and Ta across diverse environmental conditions.

In summary, our analysis revealed a dominant vegetation surface cooling effect across various phenological transitions during the growing season. By quantifying both the immediate and cumulative effects across phenological transitions, we highlight the significant role of phenological transitions in modulating vegetation foliage impacts on climate, which are influenced by background climate and interannual temperature variations. Our findings demonstrate that vegetation impact on temperature exhibits divergent trends in different regions under future climate change, emphasizing the need to incorporate phenological dynamics into climate models to improve predictions. These insights can guide climate change adaptation strategies, including the design of nature-based solutions such as afforestation, reforestation, and seasonal vegetation management to enhance cooling effects and mitigate warming impacts. Overall, our study provides a comprehensive, global perspective on the vegetation–climate feedback at the intraseasonal scale, enhancing our understanding of the biophysical processes that drive dynamic climate impact following phenological transitions.

Materials and Methods

Datasets.

Climate type dataset. To investigate the impact of phenological transitions in different background climates, we used the Köppen–Geiger climate classification (99, 100). The latest historical maps (1986–2010, https://koeppen-geiger.vu-wien.ac.at/present.htm) are based on high-resolution (101), observation-based classification consisting of 5 major climates (equatorial, arid, warm temperate, cold/boreal, and polar) and 31 subclasses. These classifications are determined by threshold values and seasonality of monthly air temperature and precipitation (102). To better examine the individual impacts of temperature and precipitation, the Köppen–Geiger climate types were further reclassified and combined based on temperature and precipitation to analyze the dominant factor in temperate and cold regions. The original climate types were reclassified into seven temperature-based types and six precipitation-based climate types. The temperature-based types include warm temperate with hot (CXa), warm (CXb), and cool summers (CXc); cold climate with hot (DXa), warm (DXb), cool summers (DXc), and extremely continental conditions (DXd), combined by the third character of the Köppen–Geiger climate classification. The precipitation-based climate types include warm temperate with fully humid (CfX), summer dry (CsX), and winter dry conditions (CwX); and cold climate with fully humid (DfX), summer dry (DsX), and winter dry conditions (DwX). We analyzed the cumulative impact of vegetation on LST and the temperature sensitivity for each climate type to examine the effects across phenological transitions and the trends as temperatures change.

VIIRS vegetation phenology product. We obtained phenological transition observations at a 500-meter resolution from the VIIRS Global Land Surface Phenology Product (GLSP) for the period of 2013–2021 (https://lpdaac.usgs.gov/products/vnp22q2v001/). VIIRS phenology product uses a Hybrid Piecewise Logistic Model (HPLM) to track the phenological transition dates by the two-band enhanced vegetation index (EVI2) (103). It defines the onset time of greenness when the EVI2 value increases during the growing season. The HPLM then fits the smoothed EVI2 trajectory by identifying transitions between green-up and senescence based on slope changes. This approach does not rely on predefined thresholds, ensuring accuracy and consistency in phenological assessments. Six key phenological transition events, including the SOS, MGP, the greenness maximum onset (GMO), the GDO, MSP, and the end of the growing season (EOS), are precisely identified through the maximum curvature change rate derived from the HPLM since 2013 (103–105). These phenological proxies are used to mark significant shifts in the phenological cycle, as detailed in *SI Appendix,* Table S2. The evaluation of VIIRS phenological data with four datasets spanning different scales suggests its precise characterization of phenological dynamics and changes (106). The study focused on regions with a single summer-peaked growing season per year. Phenological transitions were expressed as day of year (DOY), and only pixels with correctly sequenced, complete annual transitions were retained.

MODIS LST product. We used daily LST at 1 km resolution from the MODIS Aqua dataset (MYD11A1 Version 6.1, https://lpdaac.usgs.gov/products/myd11a1v061/) for 2013–2021 to characterize the effect of phenology dynamics. This dataset, retrieved using a generalized split-window algorithm for thermal bands 31 and 32 (11 and 12 μm), has undergone extensive validation (107, 108). It provides consistent and highly accurate LST estimates since 2003, enabling a better understanding of the relationship between LST and vegetation change while considering factors such as solar radiation and meteorological conditions. The Aqua dataset has two observations every day at 13:30 during the day and 03:30 at night, which are close to the highest and lowest temperatures in the diurnal cycle, respectively. We investigated the daytime LST as vegetation-induced biophysical processes primarily occur during daytime and have a greater impact on surface temperature, compared to during nighttime (8, 55), helping to investigate the maximum extent of vegetation impact. To minimize cloud contamination, we filtered the MODIS LST data using QA flags, excluding observations with cloud cover (Bits 0 to 1) or average uncertainty > 3 K. This ensured that all analyses–especially those across phenological transitions–were performed using consistent observations with minimal atmospheric interference, strengthening the reliability of our phenology-induced temperature impact.

MODIS Land cover product. The annual MODIS Land Cover Type Product (MCD12Q1 Version 6.1, 500 m spatial resolution) was utilized to identify deciduous and mixed forest pixels across the Northern Hemisphere (https://lpdaac.usgs.gov/products/mcd12q1v061/). This dataset offers a global land cover map from 2001 to the present with annual updates (109, 110). The dataset encompasses five legacy classification schemes, including the International Geosphere-Biosphere Programme (IGBP), University of Maryland (UMD), Leaf Area Index (LAI), BIOME-Biogeochemical Cycles (BGC), and Plant Functional Types (PFT). Based on the IGBP classification scheme, which divides the global land surface into 16 ecosystem types, we selected three forest types with distinct seasonal vegetation phenology for our analysis: deciduous broadleaf forests (DBF), deciduous needleleaf forests (DNF), and mixed forests (MF) (*SI Appendix,* Table S1).

AmeriFlux data. To enhance the evaluation of vegetation effects analysis at the site level, we used LST, near-surface air temperature (Ta), and ET from AmeriFlux Network (https://ameriflux.lbl.gov/). The AmeriFlux network as a core component of the global FLUXNET eddy covariance network, monitors ecosystem CO_2, water, and energy fluxes across diverse ecosystems at scales varying from local to global (111–113). The individual field sites of AmeriFlux are organized around eddy covariance flux towers (114, 115). By utilizing standardized eddy covariance instruments and data processing protocols, it provides high-resolution, noninvasive measurements of ecosystem fluxes. Since its inception, AmeriFlux flux towers have become integral to networks including the National Ecological

Observation Network (NEON), which uses a centralized, top–down approach to instrumentation and measurements (113, 116).

We used a radiative-based approach based on outgoing longwave radiation to derive half-hourly data LST from 17 AmeriFlux sites (including 11 NEON sites) characterized by deciduous broadleaf forests and mixed forest vegetation types are used in this analysis for the period 2013–2021 (*SI Appendix,* Fig. S1). The distribution of these sites aligns well with the typical climate types (CXa, DXb) considered in this study, suggesting that the site-level analysis is effectively representative. At each site, 13:30 at local time outgoing longwave radiation observations are utilized to obtain accurate LST observations, ensuring consistency and comparability with MODIS LST data. The equation used accounts for potential interferences to ensure accurate and reliable temperature data as follows:

$$L_{veg} = \frac{1}{\varepsilon_{veg}}(L_{total} - (1 - \varepsilon_{veg}) \cdot \varepsilon_{sky} \cdot L_{sky})), \quad [1]$$

where L_{veg} represents the radiance of vegetation (converted to temperature for final analysis using the Stefan–Boltzmann law), ε_{veg} is the emissivity of vegetation (assumed to be 0.97), L_{total} is the outgoing longwave radiance measured by the sensor, ε_{sky} is the emissivity of the sky (assumed to be 1), the L_{sky} is the incoming longwave radiance of the sky (117).

Time-consistent tower-based latent heat flux (LE) and Ta data at half-hour steps were used to assess the temporal dynamics of ET, Ta, and LST, evaluating surface-atmosphere thermal coupling across phenological transitions. Specifically, ET was estimated from eddy covariance measurements of LE (118), which were transformed using the latent heat of vaporization ($\lambda = 2.45$ MJ kg^{-1}) to convert into water flux (mm d^{-1}), assuming all latent energy is used for water vaporization (114, 119).

To further assess the robustness of vegetation-driven temperature signals in response to cloud presence, we conducted an additional analysis using AmeriFlux LST observations and MODIS-derived daily cloud conditions at the corresponding flux tower sites (2013–2021). Clear-sky days were identified with the same cloud-filtering criteria as above. Surface temperatures and vegetation-induced changes after phenological transitions were compared between two datasets smoothed by 5-d moving averages: one restricted to cloud-free days and the other including all daily observations.

PhenoCam data. To validate the critical role of vegetation phenology in affecting surface temperature, we utilized the ground phenological transition data from the PhenoCam Network (https://phenocam.sr.unh.edu) at the 17 AmeriFlux sites. PhenoCam Network (120) provides valuable information and imagery that can be used to characterize and monitor canopy conditions to track vegetation phenology by employing near-surface remote sensing (121, 122). PhenoCam digital camera imagery captured every 30 min from dawn to dusk, providing high-temporal-resolution measures of phenology (123, 124). For each archived image, a time series characterizes vegetation color, including "canopy greenness" with annual cycles of vegetation dynamic activity. A smoothing spline selected using the Akaike Information Criterion (AIC) is applied to the canopy greenness index to identify the baseline (minima) before the "greenness rising" phase or after the "greenness falling" phase, and the peak (maxima) between the "rising" and "falling" phases (123, 125). The dates when 10%, 25%, and 50% of the amplitude (maxima–minima) are reached in each phase are then determined (120). Given the significance of phenological transitions as well as the correspondence to VIIRS-derived phenological transitions, two key phenological transition dates were selected for the analysis: the onset of "greenness rising" (10%) corresponding to green-up onset, and the end of "greenness falling" (10%) corresponding to dormancy transition. Then the transition dates were converted to the day of the year (DOY) format and applied to filter and interpolate LST time series from AmeriFlux to capture the vegetation phenological transition effect at the site level.

Data processing. To address the differences in spatial resolution and projection among remote sensing datasets, we reprojected all datasets to the EPSG:4326 coordinate system and resampled them to a resolution of 30 km. For each grid point masked with the three selected forest types, the median values of LST and the day of year (DOY) vegetation phenological transitions were calculated each year on the GEE platform. This approach was implemented to minimize deviations and ensure consistent dataset alignment across all years. After downloading the remote sensing data from GEE and the site-level observations from AmeriFlux and PhenoCam, additional preprocessing steps were performed in R v4.3.1, including image mosaicking, pixel matching, data analysis, background climate types matching and visualization.

ATC model description. We used the ATC model to estimate the reference daily surface temperature by isolating the effect of vegetation phenological dynamics. The ATC model, originally developed for the Northern Hemisphere, offers an alternative approach for generating a continuous temperature series over a year (97, 126). The ATC model exhibits deterministic variation similar to solar irradiation and can predict daily data by using a single sinusoidal function for temporal interpolation of LST observations, as follows:

$$T(d) = T_0 + A \cdot \sin\left(\frac{2\pi d}{365} + \theta\right), \quad [2]$$

where d is the day of the temperature cycle relative to the spring equinox, and T_0, A, and θ denote the annual mean LST, the amplitude of the ATC, and the corresponding phase shift relative to the spring equinox, respectively. The robustness of the ATC model has been extensively validated globally (97, 126, 127). Due to these advantages, it has been widely used in various applications, including spatiotemporally interpolations (128–130), global LST trend analysis (131), and quantifying seasonal or interannual fluctuations in surface temperature (96, 132). The ATC model better captures annual and subseasonal LST dynamics, providing a more detailed analysis of temporal fluctuations in phenological effects on LST compared to the space-for-time substitution approach in previous studies (9, 18, 133).

Model fitting. To isolate and quantify vegetation-induced impacts on LST across phenological transitions, we implemented a two-step iteration of ATC model fitting for each vegetated pixel annually across the Northern Hemisphere.

In the first iteration, we used 5-day moving averages of MODIS and AmeriFlux observed LST (LST_{Obs}) for the full year to estimate the phase shift (θ)–defined as the timing of peak annual LST. This parameter is mainly determined by solar zenith angle and therefore using full-year data increases the robustness of this estimate. However, fitting the ATC model with year-round LST represents actual temperature with vegetation phenology influence (127, 134). To exclude the influence of vegetation-induced fluctuations, we conducted a second fitting to obtain hypothetical temperature of bare-ground-like condition without foliage interference, driven solely by the climatic background and without short-term fluctuations. Specifically, we refitted the ATC model using LST_{Obs} during the nongrowing season (i.e., period outside of the range marked by SOS or green-up onset and EOS or dormancy each pixel for each year) to capture both spatial and interannual variability in baseline LST conditions (no-foliage scenario). By reoptimizing Tâ,€ and A under radiatively consistent conditions with θ held constant, the model yields an annual baseline estimated temperature (LST_{ATC}) that represents a hypothetical seasonal temperature cycle without foliage biophysical processes at vegetated pixels. The deviation between LST_{ATC} and observed LST (LST_{Obs}) during the growing season thereby reflects the magnitude and direction of vegetation-induced temperature effects.

To quantify the impact of vegetation phenology dynamics on LST, ΔLST was derived as the difference between the MODIS and AmeriFlux observed LST (LST_{Obs}) and the ATC-estimated LST (LST_{ATC}) across the growing seasons. For both given series of observed LST values, the ATC nonlinear fitting for each pixel was estimated with the Levenberg–Marquardt algorithm (135, 136), combining the advantages of gradient descent and Newton's method to minimize the sum of squared residuals iteratively. A lower LST_{ATC} than LST_{Obs} indicates a net albedo-driven warming across phenological transitions, whereas a higher LST_{ATC} suggests net cooling from vegetation-induced ET (Fig. 1).

To investigate the impact resulting from vegetation dynamics on LST following each phenological transition in response to changes in the climate background, we calculated the sensitivity of phenological impact (ΔLST) on background temperatures using a linear regression model (*SI Appendix*, Materials).

Data, Materials, and Software Availability. All codes used to analyze data and generate figures have been deposited in GitHub (https://github.com/YizhuoLi-research/phenology-effects-on-LST) (137). All study data are included in the article and/or *SI Appendix*.

ACKNOWLEDGMENTS. Y.L. and A.W. are funded by the State Key Laboratory of Forest Ecology and Conservation, the National Key Research and Development Program (2022YFF1300501) on forest ecological product supply in Northeast China (2022–2026), and the Liaoning Province Science and Technology Attack Special Project (2023JH1/10400001) on desertification management at the southern edge of the Horqin Sandy Land (2023–2026). A.D.R. acknowledges support from NSF awards 1832210 and 2224545, A.M. funding by the

Bavarian State Ministry of Science and the Arts (bayklif project). J.M is supported by the Oak Ridge National Laboratory (ORNL) Reducing Uncertainties in Biogeochemical Interactions through Synthesis and Computing Scientific Focus Area project and the Terrestrial Ecosystem Science Scientific Focus Area project funded through the Earth and Environmental Systems Sciences Division of the Biological and Environmental Research Office in the Department of Energy Office of Science. ORNL is supported by the DOE Office of Science under Contract No. DE-AC05-00OR22725. J.D. is supported by NSF NRT fellowship (award 1829075) and NASA FINESST fellowship (award 80NSSC23K0138). Ground phenology data used in this study was provided by the PhenoCam Network, which has been supported by the NSF, the Long-Term Agroecosystem Research (LTAR) network which is supported by the United States Department of Agriculture (USDA), the U.S. Department of Energy, the U.S. Geological Survey, the Northeastern States Research Cooperative, and the USA National Phenology Network. We thank the PhenoCam Network collaborators, including site PIs and technicians, for publicly sharing the data that were used in this paper. We acknowledge the AmeriFlux sites for their data records. Funding for AmeriFlux data resources was provided by the U.S. Department of Energy's Office of Science.

Author affiliations: [a]Chinese Academy of Sciences Key Laboratory of Forest Ecology and Silviculture, Institute of Applied Ecology, Chinese Academy of Sciences, Shenyang 110016, China; [b]University of Chinese Academy of Sciences, Beijing 100049, China; [c]Department of Earth and Environmental Sciences, Vanderbilt University, Nashville, TN 37240; [d]School of Informatics, Computing and Cyber Systems, Northern Arizona University, Flagstaff, AZ 86011; [e]Center for Ecosystem Science and Society, Northern Arizona University, Flagstaff, AZ 86011; [f]School of Forestry and Environmental Studies, Yale University, New Haven, CT 06511; [g]Ecoclimatology, Technische Universität München School of Life Sciences, Technical University of Munich, 85354 Freising, Germany; [h]Institute for Advanced Study, Technical University of Munich, 85748 Garching, Germany; and [i]Environmental Sciences Division, Oak Ridge National Laboratory, Oak Ridge, TN 37830

1. A. Menzel, P. Fabian, Growing season extended in Europe. *Nature* **397**, 659–659 (1999).
2. C.-E. Park, S. Jeong, Land surface temperature sensitivity to changes in vegetation phenology over northern deciduous forests. *J. Geophys. Res. Biogeosci.* **128**, e2023JG007498 (2023).
3. X. Xu, W. J. Riley, C. D. Koven, G. Jia, X. Zhang, Earlier leaf-out warms air in the north. *Nat. Clim. Chang.* **10**, 370–375 (2020).
4. A. Menzel *et al.*, European phenological response to climate change matches the warming pattern. *Glob. Change Biol.* **12**, 1969–1976 (2006).
5. C. Körner, D. Basler, Phenology under global warming. *Science* **327**, 1461–1462 (2010).
6. S. Piao *et al.*, Leaf onset in the northern hemisphere triggered by daytime temperature. *Nat. Commun.* **6**, 6911 (2015).
7. G. Forzieri, R. Alkama, D. G. Miralles, A. Cescatti, Satellites reveal contrasting responses of regional climate to the widespread greening of Earth. *Science* **356**, 1180–1184 (2017).
8. X. Shen *et al.*, Vegetation greening, extended growing seasons, and temperature feedbacks in warming temperate grasslands of China. *J. Climate* **35**, 5103–5117 (2022).
9. Y. Li *et al.*, Local cooling and warming effects of forests based on satellite observations. *Nat. Commun.* **6**, 6603 (2015).
10. X. Lian *et al.*, Biophysical impacts of northern vegetation changes on seasonal warming patterns. *Nat. Commun.* **13**, 3925 (2022).
11. R. Alkama *et al.*, Vegetation-based climate mitigation in a warmer and greener world. *Nat. Commun.* **13**, 606 (2022).
12. Y. Li *et al.*, Biophysical impacts of earth greening can substantially mitigate regional land surface temperature warming. *Nat. Commun.* **14**, 121 (2023).
13. A. Gonsamo, J. M. Chen, Y. W. Ooi, Peak season plant activity shift towards spring is reflected by increasing carbon uptake by extratropical ecosystems. *Glob. Change Biol.* **24**, 2117–2128 (2018).
14. C. Xu, H. Liu, A. P. Williams, Y. Yin, X. Wu, Trends toward an earlier peak of the growing season in Northern Hemisphere mid-latitudes. *Glob. Change Biol.* **22**, 2852–2860 (2016).
15. T. Park *et al.*, Changes in timing of seasonal peak photosynthetic activity in northern ecosystems. *Glob. Change Biol.* **25**, 2382–2395 (2019).
16. X. Xu, W. J. Riley, C. D. Koven, G. Jia, X. Zhang, Earlier leaf-out warms air in the north. *Nat. Clim. Chang.* **10**, 370–375 (2020).
17. D. R. Fitzjarrald, V. C. Acevedo, K. E. Moore, Climatic consequences of leaf presence in the Eastern United States. *J. Climate* **14**, 598–614 (2001).
18. S. Ba *et al.*, The cooling and warming effects of potential forest transition on local land surface temperature in Northeast China. *Ecol. Indic.* **159**, 111645 (2024).
19. Y. Li *et al.*, Potential and actual impacts of deforestation and afforestation on land surface temperature. *JGR Atmos.* **121**, 14372–14386 (2016).
20. W. Shen *et al.*, Local land surface temperature change induced by afforestation based on satellite observations in Guangdong plantation forests in China. *Agric. For. Meteorol.* **276**, 107641 (2019).
21. G. Yuan *et al.*, Impacts of afforestation on land surface temperature in different regions of China. *Agric. For. Meteorol.* **318**, 108901 (2022).
22. A. F. Feldman *et al.*, Tropical surface temperature response to vegetation cover changes and the role of drylands. *Glob. Change Biol.* **29**, 110–125 (2023).
23. G. Duveiller, J. Hooker, A. Cescatti, A dataset mapping the potential biophysical effects of vegetation cover change. *Sci. Data* **5**, 180014 (2018).
24. S. Piao *et al.*, Plant phenology and global climate change: Current progresses and challenges. *Glob. Change Biol.* **25**, 1922–1940 (2019).
25. X. Lee *et al.*, Observed increase in local cooling effect of deforestation at higher latitudes. *Nature* **479**, 384–387 (2011).
26. R. Alkama, A. Cescatti, Biophysical climate impacts of recent changes in global forest cover. *Science* **351**, 600–604 (2016).
27. R. M. Bright *et al.*, Local temperature response to land cover and management change driven by non-radiative processes. *Nat. Clim. Change* **7**, 296–302 (2017).
28. Z. Zeng *et al.*, Climate mitigation from vegetation biophysical feedbacks during the past three decades. *Nat. Clim. Chang.* **7**, 432–436 (2017).
29. M. Moon, D. Li, W. Liao, A. J. Rigden, M. A. Friedl, Modification of surface energy balance during springtime: The relative importance of biophysical and meteorological changes. *Agric. For. Meteorol.* **284**, 107905 (2020).
30. M. D. Schwartz, Phenology and springtime surface-layer change. *Mon. Weather Rev.* **120**, 2570–2578 (1992).
31. X. Lian *et al.*, Biophysical impacts of northern vegetation changes on seasonal warming patterns. *Nat. Commun.* **13**, 3925 (2022).
32. X. Lian *et al.*, Biophysical impacts of northern vegetation changes on seasonal warming patterns. *Nat. Commun.* **13**, 3925 (2022).
33. D. Y. Hollinger *et al.*, Albedo estimates for land surface models and support for a new paradigm based on foliage nitrogen concentration. *Glob. Change Biol.* **16**, 696–710 (2010).
34. M. D. Schwartz, T. R. Karl, Spring phenology: Nature's experiment to detect the effect of "green-up" on surface maximum temperatures. *Mon. Wea. Rev.* **118**, 883–890 (1990).
35. Y. Zhu *et al.*, Evapotranspiration increase is more sensitive to vegetation greening than to vegetation type conversion in arid and semi-arid regions of China. *Glob. Planet. Change* **244**, 104634 (2025).
36. L. Yu *et al.*, Phenological control of vegetation biophysical feedbacks to the regional climate. *Geogr. Sustain.* **6**, 100202 (2024).
37. W. Rina *et al.*, Lagged feedback of peak season photosynthetic activities on local surface temperature in Inner Mongolia, China. *Environ. Res.* **236**, 116643 (2023).
38. Y. Jiao *et al.*, Biophysical effects of temperate forests in regulating regional temperature and precipitation pattern across Northeast China. *Remote Sens.* **13**, 4767 (2021).
39. M. Shen *et al.*, Plant phenology changes and drivers on the Qinghai–Tibetan Plateau. *Nat. Rev. Earth Environ.* **3**, 633–651 (2022).
40. C. Chen *et al.*, Biophysical impacts of Earth greening largely controlled by aerodynamic resistance. *Sci. Adv.* **6**, eabb1981 (2020).
41. Z. Liu, A. P. Ballantyne, L. A. Cooper, Increases in land surface temperature in response to fire in Siberian boreal forests and their attribution to biophysical processes. *Geophys. Res. Lett.* **45**, 6485–6494 (2018).
42. W. Liu *et al.*, Biophysical effects of paddy rice expansion on land surface temperature in northeastern Asia. *Agric. For. Meteorol.* **315**, 108820 (2022).
43. M. Pascolini-Campbell, J. T. Reager, H. A. Chandanpurkar, M. Rodell, Retraction note: A 10 per cent increase in global land evapotranspiration from 2003 to 2019. *Nature* **604**, 202–202 (2022).
44. Y. Li *et al.*, Observed different impacts of potential tree restoration on local surface and air temperature. *Nat. Commun.* **16**, 2335 (2025).
45. M. G. Windisch, E. L. Davin, S. I. Seneviratne, Prioritizing forestation based on biogeochemical and local biogeophysical impacts. *Nat. Clim. Chang.* **11**, 867–871 (2021).
46. L. Zhu *et al.*, Comparable biophysical and biogeochemical feedbacks on warming from tropical moist forest degradation. *Nat. Geosci.* **16**, 244–249 (2023).
47. K. A. Novick, G. G. Katul, The duality of reforestation impacts on surface and air temperature. *JGR Biogeosci.* **125**, e2019JG005543 (2020).
48. K. A. Novick, M. L. Barnes, A practical exploration of land cover impacts on surface and air temperature when they are most consequential. *Environ. Res. Climate* **2**, 025007 (2023).
49. K. E. Moore *et al.*, Seasonal variation in radiative and turbulent exchange at a deciduous forest in central Massachusetts. *J. Appl. Meteor.* **35**, 122–134 (1996).
50. A. D. Richardson *et al.*, Climate change, phenology, and phenological control of vegetation feedbacks to the climate system. *Agric. For. Meteorol.* **169**, 156–173 (2013).
51. E. Rotenberg, D. Yakir, Contribution of semi-arid forests to the climate system. *Science* **327**, 451–454 (2010).
52. H. P. Schmid, C. S. B. Grimmond, F. Cropley, B. Offerle, H.-B. Su, Measurements of CO2 and energy fluxes over a mixed hardwood forest in the mid-western United States. *Agric. For. Meteorol.* **103**, 357–374 (2000).
53. M. L. C. Berbet, M. H. Costa, Climate change after tropical deforestation: Seasonal variability of surface albedo and its effects on precipitation change. *J. Climate* **16**, 2099–2104 (2003).
54. H. Yan *et al.*, Forest greening increases land surface albedo during the main growing period between 2002 and 2019 in China. *J. Geophys. Res. Atmos.* **126**, e2020JD033582 (2021).
55. S.-S. Peng *et al.*, Afforestation in China cools local land surface temperature. *Proc. Natl. Acad. Sci. U.S.A.* **111**, 2915–2919 (2014).
56. D. Zhou *et al.*, Contrasting effects of urbanization and agriculture on surface temperature in eastern China. *JGR Atmos.* **121**, 9597–9606 (2016).
57. S. Li *et al.*, Seasonality of albedo and fraction of absorbed photosynthetically active radiation in the temperate secondary forest ecosystem: A comprehensive observation using Qingyuan Ker towers. *Agric. For. Meteorol.* **333**, 109418 (2023).
58. S. Ollinger, Sources of variability in canopy reflectance and the convergent properties of plants. *New Phytol.* **189**, 375–394 (2011).
59. J. E. Sanger, Quantitative investigations of leaf pigments from their inception in buds through autumn coloration to decomposition in falling leaves. *Ecology* **52**, 1075–1089 (1971).
60. S. Li *et al.*, Seasonality of albedo and fraction of absorbed photosynthetically active radiation in the temperate secondary forest ecosystem: A comprehensive observation using Qingyuan Ker towers. *Agric. For. Meteorol.* **333**, 109418 (2023).
61. A. J. Pitman *et al.*, Importance of background climate in determining impact of land-cover change on regional climate. *Nature Clim Change* **1**, 472–475 (2011).
62. G. Nan, N. Wang, L. Jiao, Y. Zhu, H. Sun, A new exploration for accurately quantifying the effect of afforestation on soil moisture: A case study of artificial *Robinia pseudoacacia* in the Loess Plateau (China). *For. Ecol. Manage.* **433**, 459–466 (2019).
63. R. M. Bright, K. Zhao, R. B. Jackson, F. Cherubini, Quantifying surface albedo and other direct biogeophysical climate forcings of forestry activities. *Glob. Change Biol.* **21**, 3246–3266 (2015).

64. X. Yuan *et al.*, Vegetation changes and land surface feedbacks drive shifts in local temperatures over Central Asia. *Sci. Rep.* **7**, 3287 (2017).
65. X. Lian *et al.*, Summer soil drying exacerbated by earlier spring greening of northern vegetation. *Sci. Adv.* **6**, eaax0255 (2020).
66. J. H. Kim *et al.*, Warming-induced earlier greenup leads to reduced stream discharge in a temperate mixed forest catchment. *JGR Biogeosci.* **123**, 1960–1975 (2018).
67. Y. Li *et al.*, Widespread spring phenology effects on drought recovery of Northern Hemisphere ecosystems. *Nat. Clim. Chang.* **13**, 182–188 (2023).
68. M. Cheng, J. Jin, H. Jiang, Strong impacts of autumn phenology on grassland ecosystem water use efficiency on the Tibetan Plateau. *Ecol. Indic.* **126**, 107682 (2021).
69. I. Garonna *et al.*, Strong contribution of autumn phenology to changes in satellite-derived growing season length estimates across Europe (1982–2011). *Glob. Change Biol.* **20**, 3457–3470 (2014).
70. Q. Wang *et al.*, Assessment of four latest long-term satellite-based precipitation products in capturing the extreme precipitation and streamflow across a humid region of southern China. *Atmos. Res.* **257**, 105554 (2021).
71. A. L. S. Swann, I. Y. Fung, J. C. H. Chiang, Mid-latitude afforestation shifts general circulation and tropical precipitation. *Proc. Nat. Acad. Sci.* **109**, 712–716 (2012).
72. M. Zhang *et al.*, Response of surface air temperature to small-scale land clearing across latitudes. *Environ. Res. Lett.* **9**, 034002 (2014).
73. S.-J. Jeong, C.-H. Ho, H.-J. Gim, M. E. Brown, Phenology shifts at start vs. end of growing season in temperate vegetation over the Northern Hemisphere for the period 1982–2008. *Glob. Change Biol.* **17**, 2385–2399 (2011).
74. R. G. Anderson *et al.*, Biophysical considerations in forestry for climate protection. *Front. Ecol. Environ.* **9**, 174–182 (2011).
75. M. U. F. Kirschbaum, Forest growth and species distribution in a changing climate. *Tree Physiol.* **20**, 309–322 (2000).
76. Z. Huang *et al.*, Belowground soil water response in the afforestation-cropland interface under semi-arid conditions. *CATENA* **193**, 104660 (2020).
77. S. I. Seneviratne *et al.*, Investigating soil moisture–climate interactions in a changing climate: A review. *Earth-Sci. Rev.* **99**, 125–161 (2010).
78. F. I. Morton, Operational estimates of areal evapotranspiration and their significance to the science and practice of hydrology. *J. Hydrol.* **66**, 1–76 (1983).
79. Z. Zhong *et al.*, Disentangling the effects of vapor pressure deficit on northern terrestrial vegetation productivity. *Sci. Adv.* **9**, eadf3166 (2023).
80. M. Forkel *et al.*, Codominant water control on global interannual variability and trends in land surface phenology and greenness. *Glob. Change Biol.* **21**, 3414–3435 (2015).
81. L. Wang *et al.*, Impact of large-scale afforestation on surface temperature: A case study in the Kubuqi Desert, Inner Mongolia based on the WRF model. *Forests* **10**, 368 (2019).
82. G. B. Bonan, Forests and climate change: Forcings, feedbacks, and the climate benefits of forests. *Science* **320**, 1444–1449 (2008).
83. L. Samaniego *et al.*, Anthropogenic warming exacerbates European soil moisture droughts. *Nat. Clim. Change.* **8**, 421–426 (2018).
84. C. Wu *et al.*, Increased drought effects on the phenology of autumn leaf senescence. *Nat. Clim. Chang.* **12**, 943–949 (2022).
85. C. Greiser *et al.*, Higher soil moisture increases microclimate temperature buffering in temperate broadleaf forests. *Agric. For. Meteorol.* **345**, 109828 (2024).
86. Y. Li *et al.*, Prioritizing forestation in China through incorporating biogeochemical and local biogeophysical effects. *Earths Future* **12**, e2024EF004536 (2024).
87. J. Schwaab *et al.*, Increasing the broad-leaved tree fraction in European forests mitigates hot temperature extremes. *Sci. Rep.* **10**, 14153 (2020).
88. V. Renaud, J. L. Innes, M. Dobbertin, M. Rebetez, Comparison between open-site and below-canopy climatic conditions in Switzerland for different types of forests over 10 years (1998–2007). *Theor. Appl. Climatol.* **105**, 119–127 (2011).
89. M. Breil, A. Weber, J. G. Pinto, The potential of an increased deciduous forest fraction to mitigate the effects of heat extremes in Europe. *Biogeosciences* **20**, 2237–2250 (2023).
90. J.-Y. Juang, G. Katul, M. Siqueira, P. Stoy, K. Novick, Separating the effects of albedo from eco-physiological changes on surface temperature along a successional chronosequence in the southeastern United States. *Geophys. Res. Lett.* **34**, 2007GL031296 (2007).
91. V. Hernandez-Santana, J. E. Fernández, C. M. Rodriguez-Dominguez, R. Romero, A. Diaz-Espejo, The dynamics of radial sap flux density reflects changes in stomatal conductance in response to soil and air water deficit. *Agric. For. Meteorol.* **218–219**, 92–101 (2016).
92. G. Wu *et al.*, Interannual variability of ecosystem iso/anisohydry is regulated by environmental dryness. *New Phytol.* **229**, 2562–2575.
93. M. Pardos *et al.*, The greater resilience of mixed forests to drought mainly depends on their composition: Analysis along a climate gradient across Europe. *For. Ecol. Manage.* **481**, 118687 (2021).
94. Y. Li, Z. Zeng, L. Huang, X. Lian, S. Piao, Comment on "Satellites reveal contrasting responses of regional climate to the widespread greening of Earth". *Science* **360**, eaap7950 (2018).
95. B. Bechtel, Robustness of annual cycle parameters to characterize the urban thermal landscapes. *IEEE Geosci. Remote Sens. Lett.* **9**, 876–880 (2012).
96. B. Bechtel, P. Sismanidis, "Time series analysis of moderate resolution land surface temperatures" in *Remote Sensing Time Series Image Processing* (CRC Press, 2018).
97. B. Bechtel, "Multitemporal Landsat data for urban heat island assessment and classification of local climate zones" in *2011 Joint Urban Remote Sensing Event* (IEEE, 2011), pp. 129–132.
98. J. M. Freedman, D. R. Fitzjarrald, K. E. Moore, R. K. Sakai, Boundary layer clouds and vegetation-atmosphere feedbacks. *J. Climate* **14**, 180–197 (2001).
99. M. Kottek, J. Grieser, C. Beck, B. Rudolf, F. Rubel, World map of the Köppen-Geiger climate classification updated. *Metz* **15**, 259–263 (2006).
100. D. Chen, H. W. Chen, Using the Köppen classification to quantify climate variation and change: An example for 1901–2010. *Environ. Dev.* **6**, 69–79 (2013).
101. F. Rubel, K. Brugger, K. Haslinger, I. Auer, The climate of the European Alps: Shift of very high resolution Köppen-Geiger climate zones 1800–2100. *metz* **26**, 115–125. (2017).
102. H. E. Beck *et al.*, High-resolution (1 km) Köppen-Geiger maps for 1901–2099 based on constrained CMIP6 projections. *Sci. Data* **10**, 724 (2023).
103. X. Zhang *et al.*, Generation and evaluation of the VIIRS land surface phenology product. *Remote Sens. Environ.* **216**, 212–229 (2018).
104. M. Li, W. Yang, A. Kondoh, Improving remote estimation of vegetation phenology using GCOM-C/SGLI land surface reflectance data. *Remote Sens.* **14**, 4027 (2022).
105. X. Zhang, M. A. Friedl, G. M. Henebry, C. Schaaf, T. Miura, VIIRS/NPP land cover dynamics yearly L3 global 500m SIN Grid V001. https://lpdaac.usgs.gov/products/vnp22q2v001/ (accessed on 12 August 2024).
106. C. Wang *et al.*, Comparison of change-based and shape-based data fusion methods in fine-resolution land surface phenology monitoring with Landsat and Sentinel-2 data. *Sci. Total Environ.* **927**, 172014 (2024).
107. Zhengming Wan, J. Dozier, A generalized split-window algorithm for retrieving land-surface temperature from space. *IEEE Trans. Geosci. Remote Sens.* **34**, 892–905 (1996).
108. S.-B. Duan *et al.*, Validation of Collection 6 MODIS land surface temperature product using in situ measurements. *Remote Sens. Environ.* **225**, 16–29 (2019).
109. T. R. Loveland *et al.*, Development of a global land cover characteristics database and IGBP DISCover from 1 km AVHRR data. *Int. J. Remote Sens.* **21**, 1303–1330 (2000).
110. M. A. Friedl *et al.*, MODIS collection 5 global land cover: Algorithm refinements and characterization of new datasets. *Remote Sens. Environ.* **114**, 168–182 (2010).
111. K. A. Novick *et al.*, The ameriflux network: A coalition of the willing. *Agric. For. Meteorol.* **249**, 444–456 (2018).
112. G. Pastorello *et al.*, The FLUXNET2015 dataset and the ONEFlux processing pipeline for eddy covariance data. *Sci. Data* **7**, 225 (2020).
113. M. Moon, A. D. Richardson, T. Milliman, M. A. Friedl, A high spatial resolution land surface phenology dataset for AmeriFlux and NEON sites. *Sci. Data* **9**, 448 (2022).
114. D. D. Baldocchi, Assessing the eddy covariance technique for evaluating carbon dioxide exchange rates of ecosystems: Past, present and future. *Glob. Change Biol.* **9**, 479–492 (2003).
115. M. L. Goulden, J. W. Munger, S.-M. Fan, B. C. Daube, S. C. Wofsy, Measurements of carbon sequestration by long-term eddy covariance: Methods and a critical evaluation of accuracy. *Glob. Change Biol.* **2**, 169–182 (1996).
116. D. Schimel, W. Hargrove, F. Hoffman, J. MacMahon, NEON: A hierarchically designed national ecological network. *Front. Ecol. Environ.* **5**, 59–59 (2007).
117. D. M. Aubrecht *et al.*, Continuous, long-term, high-frequency thermal imaging of vegetation: Uncertainties and recommended best practices. *Agric. For. Meteorol.* **228–229**, 315–326 (2016).
118. H. Chu *et al.*, AmeriFlux BASE data pipeline to support network growth and data sharing. *Sci. Data* **10**, 614 (2023).
119. A. G. Richard, P. S. Luis, R. Dirk, S. Martin, Crop evapotranspiration – Guidelines for computing crop water requirements. *FAO Irrigation and Drainage Paper No. 56* (1998).
120. A. D. Richardson *et al.*, Tracking vegetation phenology across diverse North American biomes using PhenoCam imagery. *Sci. Data* **5**, 180028 (2018).
121. B. Seyednasrollah *et al.*, Tracking vegetation phenology across diverse biomes using version 2.0 of the PhenoCam dataset. *Sci. Data* **6**, 222 (2019).
122. A. D. Richardson, K. Hufkens, T. Milliman, S. Frolking, Intercomparison of phenological transition dates derived from the PhenoCam Dataset V1.0 and MODIS satellite remote sensing. *Sci. Rep.* **8**, 5679 (2018).
123. O. Sonnentag *et al.*, Digital repeat photography for phenological research in forest ecosystems. *Agric. For. Meteorol.* **152**, 159–177 (2012).
124. A. D. Richardson *et al.*, Use of digital webcam images to track spring green-up in a deciduous broadleaf forest. *Oecologia* **152**, 323–334 (2007).
125. C. M. Hurvich, J. S. Simonoff, C.-L. Tsai, Smoothing parameter selection in nonparametric regression using an improved Akaike information criterion. *J. R. Stat. Soc. Ser. B Stat. Methodol.* **60**, 271–293 (1998).
126. B. Bechtel, A new global climatology of annual land surface temperature. *Remote Sensing* **7**, 2850–2870 (2015).
127. Z. Zou *et al.*, Enhanced modeling of annual temperature cycles with temporally discrete remotely sensed thermal observations. *Remote Sensing* **10**, 650 (2018).
128. J. Quan *et al.*, A hybrid method combining neighborhood information from satellite data with modeled diurnal temperature cycles over consecutive days. *Remote Sens. Environ.* **155**, 257–274 (2014).
129. W. Zhan *et al.*, Remotely sensed soil temperatures beneath snow-free skin-surface using thermal observations from tandem polar-orbiting satellites: An analytical three-time-scale model. *Remote Sens. Environ.* **143**, 1–14 (2014).
130. P. Sismanidis, B. Bechtel, I. Keramitsoglou, C. T. Kiranoudis, Mapping the spatiotemporal dynamics of Europe's land surface temperatures. *IEEE Geosci. Remote Sensing Lett.* **15**, 202–206 (2018).
131. Z. Xing *et al.*, Estimation of daily mean land surface temperature at global scale using pairs of daytime and nighttime MODIS instantaneous observations. *ISPRS J. Photogramm. Remote Sens.* **178**, 51–67 (2021).
132. P. Fu, Q. Weng, Variability in annual temperature cycle in the urban areas of the United States as revealed by MODIS imagery. *ISPRS J. Photogramm. Remote Sens.* **146**, 65–73 (2018).
133. L. Wang *et al.*, Response of surface temperature to afforestation in the Kubuqi Desert, Inner Mongolia. *J. Geophys. Res. Atmos.* **123**, 948–964 (2018).
134. A. R. Stine, P. Huybers, I. Y. Fung, Changes in the phase of the annual cycle of surface temperature. *Nature* **457**, 435–440 (2009).
135. J. J. Moré, "The Levenberg-Marquardt algorithm: Implementation and theory", in *Lecture Notes in Mathematics, Numerical Analysis*, G. A. Watson, Ed. (Springer, Berlin Heidelberg, 1978), pp. 105–116.
136. H. P. Gavin, The Levenberg-Marquardt algorithm for nonlinear least squares curve-fitting problems. *Depart. Civil Environ. Eng. Duke University* **3**, 1–19 (2019).
137. Y. Li *et al.*, Data from "Cooling outweighs warming across phenological transitions in the Northern Hemisphere." GitHub. https://github.com/YizhuoLi-research/phenology-effects-on-LST. Deposited 23 January 2025.